Probing two-electron multiplets in bilayer graphene quantum dots

DOI:
10.1103/PhysRevLett.127.256802

Document Version
Final published version

Editors' Suggestion

Probing Two-Electron Multiplets in Bilayer Graphene Quantum Dots

S. Möller,[1,2] L. Banszerus,[1,2] A. Knothe,[3] C. Steiner,[1] E. Icking,[1,2] S. Trellenkamp,[4] F. Lentz,[4] K. Watanabe,[5] T. Taniguchi,[6] L. I. Glazman,[7] V. I. Fal'ko,[3,8,9] C. Volk,[1,2] and C. Stampfer[1,2,*]

[1]*JARA-FIT and 2nd Institute of Physics, RWTH Aachen University, Aachen 52074, Germany*
[2]*Peter Grünberg Institute (PGI-9), Forschungszentrum Jülich, Jülich 52425, Germany*
[3]*National Graphene Institute, University of Manchester, Manchester M13 9PL, United Kingdom*
[4]*Helmholtz Nano Facility, Forschungszentrum Jülich, Jülich 52425, Germany*
[5]*Research Center for Functional Materials, National Institute for Materials Science, 1-1 Namiki, Tsukuba 305-0044, Japan*
[6]*International Center for Materials Nanoarchitectonics, National Institute for Materials Science, 1-1 Namiki, Tsukuba 305-0044, Japan*
[7]*Departments of Physics and Applied Physics, Yale University, New Haven, Connecticut 06520, USA*
[8]*Department of Physics and Astronomy, University of Manchester, Oxford Road, Manchester M13 9PL, United Kingdom*
[9]*Henry Royce Institute for Advanced Materials, University of Manchester, Manchester M13 9PL, United Kingdom*

(Received 16 June 2021; accepted 1 November 2021; published 15 December 2021)

We report on finite bias spectroscopy measurements of the two-electron spectrum in a gate defined bilayer graphene (BLG) quantum dot for varying magnetic fields. The spin and valley degree of freedom in BLG give rise to multiplets of six orbital symmetric and ten orbital antisymmetric states. We find that orbital symmetric states are lower in energy and separated by $\approx$ 0.4–0.8 meV from orbital antisymmetric states. The symmetric multiplet exhibits an additional energy splitting of its six states of $\approx$ 0.15–0.5 meV due to lattice scale interactions. The experimental observations are supported by theoretical calculations, which allow to determine that intervalley scattering and "current-current" interaction constants are of the same magnitude in BLG.

DOI: 10.1103/PhysRevLett.127.256802

Graphene quantum dots (QDs) are considered promising candidates for spin-based quantum computation, as the low spin-orbit and hyperfine coupling provides long spin coherence times [1–5]. In addition to the spin, graphene offers the valley degree of freedom, which gives rise to a rich energy spectrum and creates the opportunity for the implementation of valley and Kramer's qubits [5–7]. Recent experimental progress on electrostatically confined bilayer graphene (BLG) QDs, demonstrating single-electron occupation [8–10], gate-tunable valley g factors [11] and low spin-orbit coupling [12–14], brings graphene-based qubits within reach. As two-electron states are particularly interesting for the implementation of well-controllable qubits, such as exchange and singlet-triplet qubits [15,16], which offer various advantages over single-electron qubits, a detailed understanding of the two-particle spectrum in BLG QDs is becoming increasingly important.

This is all the more true since the spin and valley (K^+, K^-) degrees of freedom in BLG yield a total of 16 two-particle states where the wave-function-dependent valley g factors give rise to a rich level spectrum. The total two-particle wave function in BLG can be factorized into an orbital, a spin and a valley term [17,18], resulting in six states with an antisymmetric spin valley and a symmetric orbital wave function, and ten states with a symmetric spin-valley and an antisymmetric orbital wave function. This gives rise to the symmetric and antisymmetric multiplet structure of the two-electron spectrum in BLG.

In this Letter, we report on the experimental observation and detailed description of the symmetric and antisymmetric two-electron multiplets in BLG QDs. We confirm the Berry curvature induced wave function dependence of the valley magnetic moment, observing different valley g factors for single-particle, symmetric, and antisymmetric orbital wave functions, which gives rise to a rich magnetic-field dependent transition structure. Additionally, we show that the energy splitting between the multiplets (Δ_{Orb}) can be tuned in the range of 0.4–0.8 meV and that the splitting of the orbital-symmetric multiplet allows us to quantify inherent lattice scale interaction constants in BLG [19–21].

We reconstruct the two-electron spectrum of the BLG QD from finite bias spectroscopy measurements of the $\mathcal{N} = 1 \rightarrow 2$ transition. Therefore, it is necessary to consider both single- and two-particle states, which are presented in Figs. 1(a), 1(b). Figure 1(b) shows the energy of the four single-particle states of the lowest orbital as a function of an out-of-plane magnetic field, $B_\perp$. At zero magnetic field, the four states are split into two Kramers pairs by Kane-Mele spin-orbit coupling, Δ_{SO}, [12–14,22]. At finite magnetic field, the states shift linearly in energy according to their spin and valley Zeeman

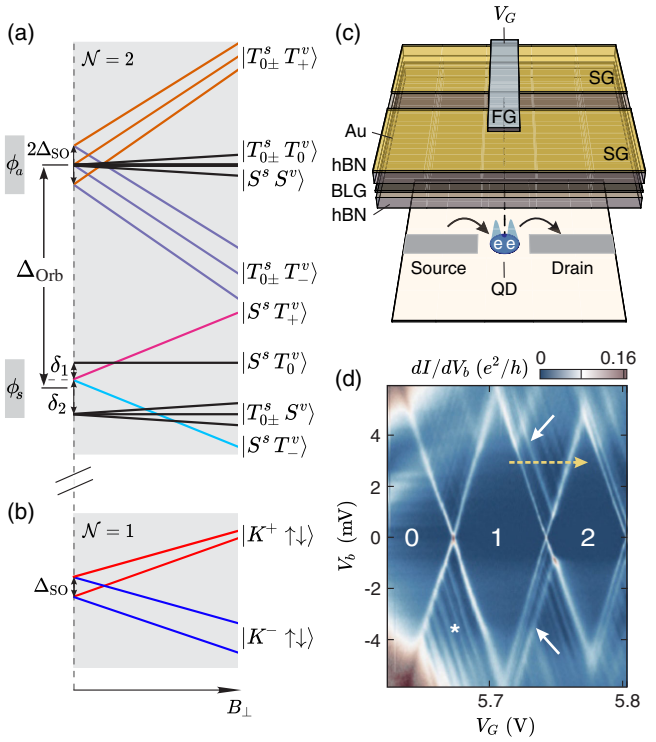

FIG. 1. (a), (b) Single-, $\mathcal{N}=1$, and two-particle, $\mathcal{N}=2$, energy spectrum of a BLG QD in an out-of-plane magnetic field. The two-particle states are split into two multiplets with (anti)symmetric orbital wave function, (ϕ_a) ϕ_s, consisting of (ten) six states. They are separated by an orbital splitting, Δ_{Orb}, while the symmetric multiplet is split again, denoted with $\delta_{1,2}$. The valley g factor is different for single-particle, symmetric, and antisymmetric orbitals. (c) Schematic of the device with BLG encapsulated in hexagonal boron nitride and multiple gate layers that create the QD via soft confinement. (d) Differential conductance dI/dV_b with respect to applied bias and FG voltage, showing diamond shaped regions of Coulomb blockade. Finite bias measurements are performed along the yellow arrow to inspect the excited state spectrum in the single and two-particle regime. White arrows highlight excited states of the two-particle spectrum.

effect $\Delta E(B_\perp)=\frac{1}{2}(\pm g_s\pm g_v^{(1)})\mu_B B_\perp$, with the spin g factor $g_s=2$, the single-particle (wave function dependent) valley g factor $g_v^{(1)}$, and the Bohr magneton μ_B [17,23–25]. Note that the valley g factor is usually around one order of magnitude larger than the spin g factor. Measurements confirming the well-understood single-electron spectrum in our single QD are shown in Supplemental Material, Fig. S2 [26]. The 16 two-particle states are shown in Fig. 1(a), which, at $B_\perp=0$, group into the orbital symmetric (ϕ_s) and antisymmetric (ϕ_a) multiplets separated by the energy Δ_{Orb}. For both the valley and spin wave function components, there are three symmetric and one antisymmetric two-particle states, namely the triplets $|T^{s,v}_{0\pm}\rangle$ and the singlet $|S^{s,v}\rangle$, where s and v refer to spin and valley. There are six (ten) antisymmetric (symmetric) combinations of the spin and valley components, which need to be combined with an (anti)symmetric orbital component for the total wave function to remain antisymmetric [27]. The orbital energy of the two-particle states comprises the occupied single-particle orbitals' energies and Coulomb interactions between the two particles, which lead to a splitting of symmetric and antisymmetric orbitals by Δ_{Orb}, depending on the size of the QD, surrounding screening and applied displacement field [17]. Additionally, the orbitally symmetric states are affected by short-range Coulomb interactions inherent to BLG [19–21], since their orbital wave functions have nonzero density at the relevant short interparticle distances. BLG exhibits local density fluctuations that are determined by the lattice symmetry. Mutual interactions between these fluctuations induce the formation of states with spontaneously broken symmetries in sublattice and valley space, introducing splittings $\delta_{1,2}$ proportional to the strength of the corresponding short-range interactions [18]. The energy of the spin- and valley-dependent part is determined by the coupling to the magnetic field and the spin-orbit coupling. Kane-Mele spin-orbit coupling induces opposite spin splittings in the two valleys, which only affects states in the antisymmetric orbital that are both valley and spin polarized. A perpendicular magnetic field couples to spin- and/or valley-polarized states $|T^{v,s}_{0\pm}\rangle$ and shifts their energies according to their corresponding g factors. Note, that the two-particle valley g factors (g_v^s, g_v^a) are in general also different from the single-particle g factor $(g_v^{(1)})$ [28].

Figure 1(c) shows a schematic of our QD device, which consists of a BLG flake encapsulated in hexagonal boron nitride (hBN). This heterostructure is placed on a graphite back gate (BG) and has two Cr/Au gate layers evaporated on top, a set of split gates (SG) and a finger gate (FG). To form a QD, we follow previous works [8–11,13,24,29,30]: A narrow p-doped channel is created utilizing SG and BG. The FG locally overcompensates the potential applied by the BG to form an n-type QD. It is separated from source and drain by two tunneling barriers, where the Fermi energy resides within the band gap. With a simple plate capacitor model [31], we estimate the radius of our QD to be $\approx$ 80 nm, which is compatible with the dimensions of the gate layout.

Figure 1(d) shows the differential conductance, dI/dV_b, through the QD as a function of the bias, V_b, and FG voltage, V_G, for an electron occupation, $\mathcal{N}$, between zero and two. Within the Coulomb diamonds, $\mathcal{N}$ is fixed and transport is suppressed by Coulomb blockade. The outline of the conducting region between $\mathcal{N}=1$ and $\mathcal{N}=2$ is defined by the ground state (GS) transition entering and leaving the bias window. Here, "GS transition" refers to the QD being in its GS before and after the tunneling of the second electron onto the QD. Additional transitions involving excited states (ES) of the $\mathcal{N}=1$ and/or $\mathcal{N}=2$ spectrum are possible within that region, as highlighted

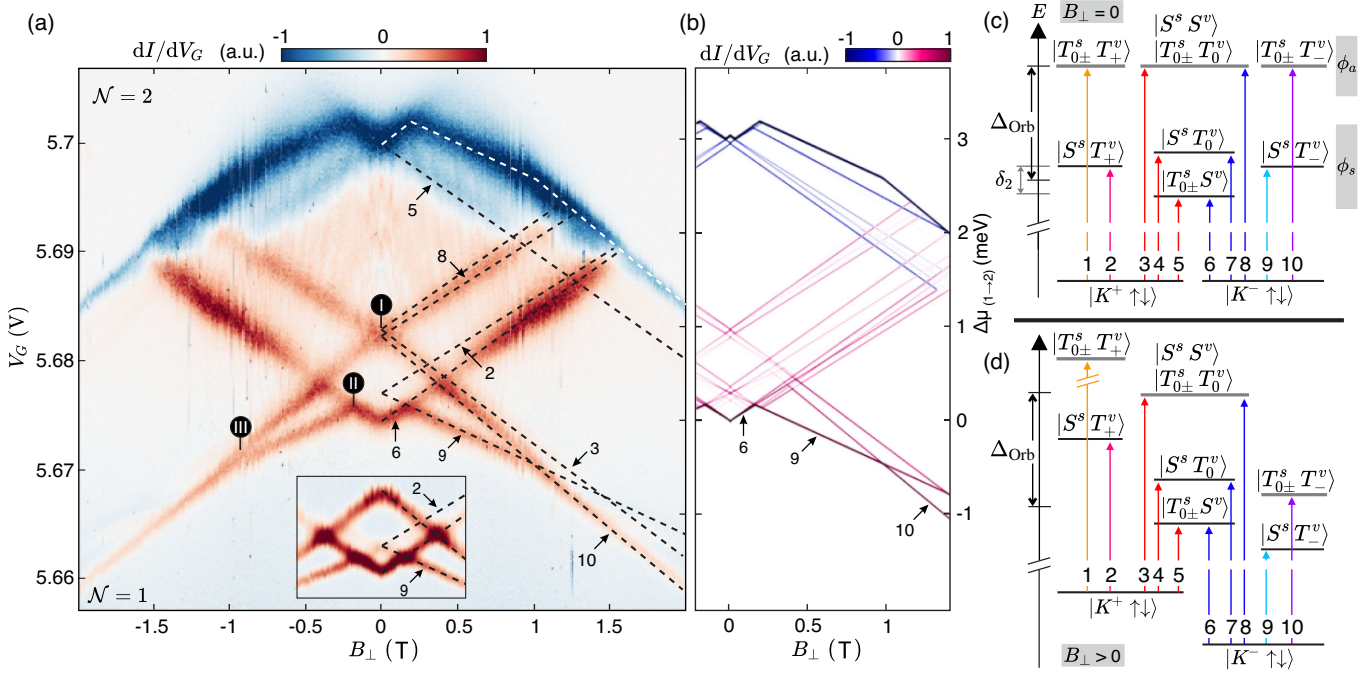

FIG. 2. (a) Differential transconductance dI/dV_G as a function of V_G and $B_\perp$, measured across the $\mathcal{N}=2$ Coulomb peak at $V_b = 3$ mV as indicated in Fig. 1(b). Transitions to states with symmetric and antisymmetric orbital wave function with different g factors give rise to a rich spectrum. The inset shows an enlargement for low magnetic field with reversed bias, where the multiplet splitting is visible. Prominent features are highlighted by dashed lines, obtained from theoretically predicted features in (b): calculated differential conductance map as in (a), assuming $g_v^{(1)} = 39$, $g_v^s = 32$, $g_v^a = 43$, $\Delta_{\rm SO} = 80$ μeV, $\delta_1 = 66$ μeV, $\delta_2 = 306$ μeV, and an asymmetry of the tunnel barriers to source t^S and drain t^D of $t^S/t^D = 0.7$. (c),(d) Transition scheme from one to two electrons in the QD at zero (c) and finite (d) $B_\perp$, with spin-orbit coupling and spin Zeeman splittings omitted for simplicity. The length of the transition arrows corresponds to the chemical potential necessary to enter the second electron in the QD, which also corresponds to the y axis in (a) and (b).

by the white arrows. Apart from QD transitions, we also observe additional features in the differential conductance in Fig. 1(d) [32], which most likely originate from density of states effects in the leads [33,34] (see white asterisk) and have previously been observed in similar devices [24].

To experimentally investigate the two-particle spectrum, we measure line cuts along the dashed arrow in Fig. 1(d) and inspect the magnetic field dependence of the GS and ES transitions. In Fig. 2(a), we plot the transconductance, dI/dV_G, at $V_b = 3$ mV as function of V_G and $B_\perp$. The gate voltage along the dashed arrow in Fig. 1(d) was converted to electrochemical potential [displayed on the right axis of Fig. 2(b)] and the raw data was corrected for magnetic field dependent oscillations in the lever arm, which are due to Shubnikov–de Haas oscillations in the lead region [25]. With increasing V_G, first the GS transition enters the bias window, then additional transitions follow, each appearing as feature of increased differential transconductance, giving rise to a rich spectrum. Eventually, the GS transition leaves the bias window, which Coulomb blockades the QD and appears as a feature of strong negative transconductance (white dashed line). The inset shows the reversed bias direction for low magnetic fields [35]. From the linewidth of the features, we may estimate a lower bound for possible spin and/or valley mixing of < 100 μeV, in good agreement with recent measurements on BLG double QDs [13].

We reproduce the features of Fig. 2(a) in theoretical calculations, which are shown in Fig. 2(b). Tunneling transport through the QD is described by solving the rate equations for the single- and two-particle states presented in Figs. 1(a) and 1(b) [36]. We obtain the tunnel rates for a single-electron sequential tunnelling process to first order in the tunneling Hamiltonian and by applying Fermi's golden rule. Using the tunnel rates we compute the occupation probabilities for the different QD states in the stationary limit and the resulting sequential tunnelling current. Employing this procedure and adjusting the free parameters $g_v^{(1)}$, $g_v^{s,a}$, $\delta_{1,2}$, $t^{S,D}$, and $\Delta_{\rm SO}$, we obtain differential transconductance maps [18] as in Fig. 2(b).

Now, we assign the most prominent features in Figs. 2(a) and 2(b) to their corresponding transitions from single- to two-particle states. Figure 2(c) shows all possible transitions at zero magnetic field, where the spin-orbit splitting was neglected for simplicity. The length of each transition arrow directly corresponds to the chemical potential required for that transition. Identifying transitions with the features in Fig. 2(a) allows us to extract the involved

energy scales. The orbital splitting is $\Delta_{\mathrm{Orb}} \approx 700\ \mu$eV, with the symmetric orbital providing the GS transition (5,6) and the antisymmetric orbital appearing at position (I) with transitions 1, 3, 8, and 10. From the inset in Fig. 2(a), we can extract $\delta_2 \approx 350\ \mu$eV, while $\delta_1 \approx 0$ within the measurement resolution. Figure 2(d) shows the level scheme at finite $B_\perp$. We can identify three different slopes that match neatly with the data. The first ones are caused by transitions where only the single-particle states shift with $g_v^{(1)}$ and the two-particle states remain constant (3-8), while the other two are due to transitions from the single-particle states to the valley polarized triplets in either the symmetric (2,9) or antisymmetric (1,10) orbital [42]. The change in chemical potential for each transition is given by $\Delta\mu_{3-8} = \pm\frac{1}{2}g_v^{(1)}\mu_B B_\perp$, $\Delta\mu_{2,9} = \pm(g_v^s - \frac{1}{2}g_v^{(1)})\mu_B B_\perp$, and $\Delta\mu_{1,10} = \pm(g_v^a - \frac{1}{2}g_v^{(1)})\mu_B B_\perp$, respectively.

Taking these different slopes into account, it can be understood how the GS transition evolves with magnetic field. Transitions 5 and 6 are the GS transition for zero magnetic field. For increasing positive magnetic field, transition 6 requires more chemical potential, while transition 5 needs less. Still, transition 6 remains the GS transition (which defines the Coulomb blockaded region), since $|K^-\rangle$ is the single-particle GS. Instead, transition 5 becomes a "negative" excited state, which manifests as a decrease in transconductance [see arrow 5 in Fig. 2(a)]. At position (II), transition 9 becomes the GS transition, when $|S^s T^v_-\rangle$ becomes the two-particle GS. This reveals that the symmetric orbital is lower in energy than the antisymmetric one, since only the multiplet splitting of the symmetric orbital gives rise to this change in the GS transition. When further increasing the magnetic field, transition 10 eventually becomes the GS transition [see position (III)], as soon as $|T^s_{0\pm}T^v_-\rangle$ is lower in energy than $|S^s T^v_-\rangle$, showing that $g_v^a > g_v^s$.

In order to better understand the energy scales involved in the two-particle spectrum, the measurement of Fig. 2(a) is performed for different displacement fields, D, applied to the BLG, which changes the band structure and also the confinement potential of the QD [17]. For each displacement field, we evaluated $\Delta_{\mathrm{Orb}}, \delta_2$, and the valley g factors of the most distinct transitions. For transitions 3–8 in Fig. 2, the slope only arises from the single-particle states, since the two-particle states do not shift with magnetic field. Figure 3(a) shows that the single-particle g factor evaluated from transitions 6 and 8 are the same within the error margins, even though they target states in two different orbitals. There is a decrease of $g_v^{(1)}$ for higher displacement fields, which was also observed earlier [11]. This decrease is also visible in Fig. 3(b), where the g factors of the symmetric and antisymmetric orbitals $g_v^{s,a}$, are evaluated from transitions 9 and 10. They show an average difference of $g_v^a - g_v^s \approx 8$, confirming that the symmetric and antisymmetric orbital comprise of different single-particle orbital states. The decrease of all g factors in Fig. 3 indicates a shift in the wave functions' composition in k space. This conclusion is supported by the fact that both the orbital splitting as well as the short range interaction contribution δ_2 show the same trend in Fig. 3(c), since they also scale with the shape of the wave function [17]. The orbital splitting, Δ_{Orb}, decreases from ≈ 0.8 to 0.4 meV for increasing displacement fields, while δ_2 decreases from ≈ 0.5 to 0.15 meV. For all displacement fields, $\delta_1 \approx 0$ within the measurement resolution.

The measurements of the splittings in Fig. 3(c) allow conclusions about the microscopic short-range interaction constants in BLG. We can relate the multiplet splittings $\delta_{1,2}$ to the short-range coupling constants [18–20], $g_\perp$, (quantifying intervalley scattering) and, g_{z0}, g_{0z} (generated by "current-current" interactions): $\delta_1 + \delta_2 = 8|g_\perp \mathfrak{F}|$ and $\delta_2 - \delta_1 = 4|(g_{z0} + g_{0z})\mathfrak{F}|$. The influence of the QD size, confinement potential and band gap on the short-range splitting is captured in $\mathfrak{F}$, which is the wave function overlap of the specific QD state [17,18]. Consequently,

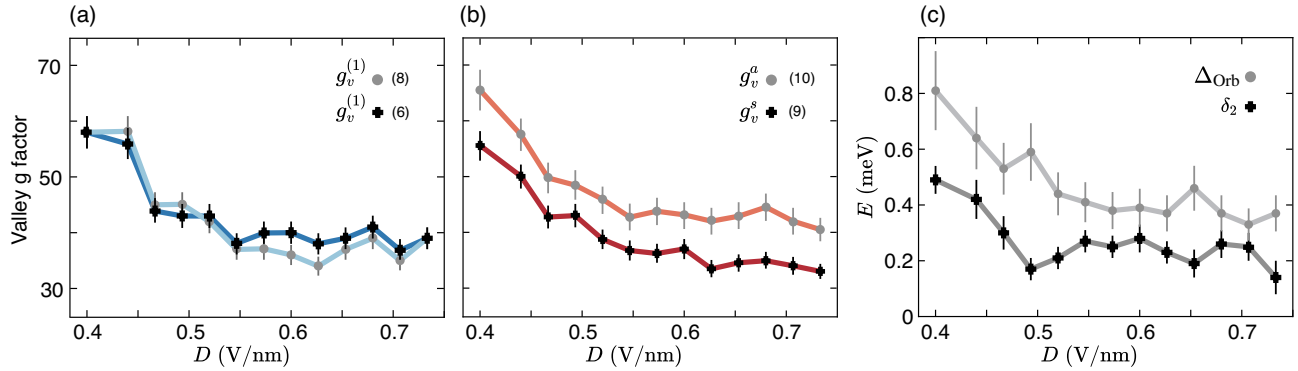

FIG. 3. (a) Single-particle g factors, $g_v^{(1)}$, as a function of applied perpendicular displacement field, evaluated from transitions to orbitally symmetric (six) or antisymmetric (eight) two-particle states with vanishing valley magnetic moment [labeling as in Fig. 2(c)]. (b) Two-particle g factors, $g_v^{s,a}$, evaluated from the transitions to valley triplet states in the (anti)symmetric orbital. Symmetric and antisymmetric orbitals exhibit an average g factor difference of ≈ 8. (c) Energy splitting between symmetric and antisymmetric orbital, Δ_{Orb}, and multiplet splitting, δ_2, in the symmetrical orbital as a function of displacement field.

our experimental observation of near-vanishing δ_1 indicates that intervalley scattering and "current-current" interactions are of the same magnitude in BLG QDs, i.e., $2|g_\perp| \approx |g_{z0} + g_{0z}|$. Calculating $\mathfrak{F}$ for QDs of radius $\approx$ 80 nm yields $\mathfrak{F} \approx 4 \times 10^{-4}$ nm^{-2} [17]. Combining this with our experimental results for δ_2, we obtain an estimate for the short-range BLG coupling constants [43], $|g_\perp| \approx 0.08$ eV nm^2, which is in accordance with the order of magnitude estimated previously from microscopic calculations [17].

In summary, we have experimentally observed both orbitally symmetric and antisymmetric two-particle states in a BLG QD using finite bias tunneling spectroscopy. We identified that the 16 possible states are split into orbitally symmetric and antisymmetric two-particle states separated by $\Delta_{\mathrm{Orb}} \approx 0.4$–$0.8$ meV. The orbitally symmetric multiplet is further split with $\delta_2 \approx 0.15$–0.5 meV by lattice scale interactions which are equally related to intervalley scattering and "current-current" interactions. We find that the two-particle ground state is a spin triplet at $B = 0$ but can be tuned to be a spin singlet for finite out-of-plane magnetic field. This is in contrast to semiconductor QDs, where the spin singlet is the two-particle ground state for common magnetic field strengths and is utilized for qubit readout in double QDs via Pauli spin blockade. Understanding the two-particle spectrum in BLG QDs is thus an essential step for further investigating the influence of the valley on Pauli blockade in double QDs and eventually for identifying a suitable regime for qubit operations.

This project has received funding from the European Union's Horizon 2020 research and innovation programme under Grant Agreement No. 881603 (Graphene Flagship) and from the European Research Council (ERC) under Grant Agreement No. 820254, the Deutsche Forschungsgemeinschaft (DFG, German Research Foundation) under Germany's Excellence Strategy—Cluster of Excellence Matter and Light for Quantum Computing (ML4Q) EXC 2004/1—390534769, through DFG (STA 1146/11-1), and by the Helmholtz Nano Facility [44]. V. I. F. and A. K. were supported by EC-FET Core 3 European Graphene Flagship Project, EC-FET Quantum Flagship Project 2D-SIPC, and Lloyd Register Foundation Nanotechnology Grant. L. I. G. was supported by the NSF DMR-2002275. Growth of hexagonal boron nitride crystals was supported by the Elemental Strategy Initiative conducted by the MEXT, Japan, Grant No. JPMXP0112101001, JSPS KAKENHI Grant No. JP20H00354 and the CREST(JPMJCR15F3), JST.

S. M. and L. B. contributed equally to this work.

*stampfer@physik.rwth-aachen.de

[1] D. Loss and D. P. DiVincenzo, Phys. Rev. A **57**, 120 (1998).
[2] C. H. Bennett and D. P. DiVincenzo, Nature (London) **404**, 247 (2000).
[3] B. Trauzettel, D. V. Bulaev, D. Loss, and G. Burkard, Nat. Phys. **3**, 192 (2007).
[4] P. G. Silvestrov and K. B. Efetov, Phys. Rev. Lett. **98**, 016802 (2007).
[5] N. Rohling and G. Burkard, New J. Phys. **14**, 083008 (2012).
[6] N. Rohling, M. Russ, and G. Burkard, Phys. Rev. Lett. **113**, 176801 (2014).
[7] E. A. Laird, F. Kuemmeth, G. A. Steele, K. Grove-Rasmussen, J. Nygård, K. Flensberg, and L. P. Kouwenhoven, Rev. Mod. Phys. **87**, 703 (2015).
[8] M. Eich, F. Herman, R. Pisoni, H. Overweg, A. Kurzmann, Y. Lee, P. Rickhaus, K. Watanabe, T. Taniguchi, M. Sigrist, T. Ihn, and K. Ensslin, Phys. Rev. X **8**, 031023 (2018).
[9] L. Banszerus, S. Möller, E. Icking, K. Watanabe, T. Taniguchi, C. Volk, and C. Stampfer, Nano Lett. **20**, 2005 (2020).
[10] L. Banszerus, A. Rothstein, T. Fabian, S. Möller, E. Icking, S. Trellenkamp, F. Lentz, D. Neumaier, K. Watanabe, T. Taniguchi, F. Libisch, C. Volk, and C. Stampfer, Nano Lett. **20**, 7709 (2020).
[11] C. Tong, R. Garreis, A. Knothe, M. Eich, A. Sacchi, K. Watanabe, T. Taniguchi, V. Fal'ko, T. Ihn, K. Ensslin, and A. Kurzmann, Nano Lett. **21**, 1068 (2021).
[12] L. Banszerus, B. Frohn, T. Fabian, S. Somanchi, A. Epping, M. Muller, D. Neumaier, K. Watanabe, T. Taniguchi, F. Libisch, B. Beschoten, F. Hassler, and C. Stampfer, Phys. Rev. Lett. **124**, 177701 (2020).
[13] L. Banszerus, S. Möller, C. Steiner, E. Icking, S. Trellenkamp, F. Lentz, K. Watanabe, T. Taniguchi, C. Volk, and C. Stampfer, Nat. Commun. **12**, 5250 (2021).
[14] A. Kurzmann, Y. Kleeorin, C. Tong, R. Garreis, A. Knothe, M. Eich, C. Mittag, C. Gold, F. K. de Vries, K. Watanabe, T. Taniguchi, V. Fal'ko, Y. Meir, T. Ihn, and K. Ensslin, arXiv:2103.04864.
[15] J. Medford, J. Beil, J. M. Taylor, E. I. Rashba, H. Lu, A. C. Gossard, and C. M. Marcus, Phys. Rev. Lett. **111**, 050501 (2013).
[16] J. R. Petta, A. C. Johnson, J. M. Taylor, E. A. Laird, A. Yacoby, M. D. Lukin, C. M. Marcus, M. P. Hanson, and A. C. Gossard, Science **309**, 2180 (2005).
[17] A. Knothe and V. Fal'ko, Phys. Rev. B **101**, 235423 (2020).
[18] A. Knothe, L. I. Glazman, and V. I. Fal'ko, arXiv:2104.03399.
[19] Y. Lemonik, I. Aleiner, and V. I. Fal'ko, Phys. Rev. B **85**, 245451 (2012).
[20] Y. Lemonik, I. L. Aleiner, C. Toke, and V. I. Fal'ko, Phys. Rev. B **82**, 201408(R) (2010).
[21] I. L. Aleiner, D. E. Kharzeev, and A. M. Tsvelik, Phys. Rev. B **76**, 195415 (2007).
[22] C. L. Kane and E. J. Mele, Phys. Rev. Lett. **95**, 226801 (2005).
[23] A. Knothe and V. Fal'ko, Phys. Rev. B **98**, 155435 (2018).
[24] M. Eich, R. Pisoni, A. Pally, H. Overweg, A. Kurzmann, Y. Lee, P. Rickhaus, K. Watanabe, T. Taniguchi, K. Ensslin, and T. Ihn, Nano Lett. **18**, 5042 (2018).
[25] L. Banszerus, T. Fabian, S. Möller, E. Icking, H. Heiming, S. Trellenkamp, F. Lentz, D. Neumaier, M. Otto, K. Watanabe, T. Taniguchi, F. Libisch, C. Volk, and C. Stampfer, Phys. Status Solidi B **257**, 2000333 (2020).

[26] See the Supplemental Material at http://link.aps.org/supplemental/10.1103/PhysRevLett.127.256802 for additional experimental data and a detailed description of our theoretic model.
[27] F. Pei, E. A. Laird, G. A. Steele, and L. P. Kouwenhoven, Nat. Nanotechnol. **7**, 630 (2012).
[28] The simplest ϕ_s would be that both charge carriers are in the lowest energy single-particle orbital. In that case, the valley g factors would be the same for the symmetric two-particle and single-particle wave functions. Conversely, a differing g factor indicates that also higher energy single-particle orbital states are included in ϕ_s.
[29] L. Banszerus, B. Frohn, A. Epping, D. Neumaier, K. Watanabe, T. Taniguchi, and C. Stampfer, Nano Lett. **18**, 4785 (2018).
[30] A. Kurzmann, M. Eich, H. Overweg, M. Mangold, F. Herman, P. Rickhaus, R. Pisoni, Y. Lee, R. Garreis, C. Tong, K. Watanabe, T. Taniguchi, K. Ensslin, and T. Ihn, Phys. Rev. Lett. **123**, 026803 (2019).
[31] We use $E_C = e^2 \cdot d_{\mathrm{hBN}}/(\pi\epsilon_0\epsilon_{\mathrm{hBN}} r_{\mathrm{QD}}^2)$, with the charging energy E_C, the dielectric permittivity of hBN, $\epsilon_{\mathrm{hBN}} \approx 4$, the thickness of the hBN, d_{hBN} and the radius of the QD, r_{QD}.
[32] All features originating from the QD should be symmetric in bias as long as tunnel barriers are not too asymmetric.
[33] A. Manna, B. Muralidharan, and S. Mahapatra, arXiv:1712.04168.
[34] F. S. Thomas, M. Nilsson, C. Ciaccia, C. Jünger, F. Rossi, V. Zannier, L. Sorba, A. Baumgartner, and C. Schönenberger, Phys. Rev. B **104**, 115415 (2021).
[35] Due to slight asymmetries in the applied bias, probably due to the tunnel barriers, different features are more prominent at reversed bias.
[36] The model for the QD, the leads, and the QD-lead tunnel coupling are presented in [26], which includes Refs. [17,19,20,25,37–41].
[37] H. Ochoa, A. H. Castro Neto, V. I. Fal'ko, and F. Guinea, Phys. Rev. B **86**, 245411 (2012).
[38] D. Xiao, M.-C. Chang, and Q. Niu, Rev. Mod. Phys. **82**, 1959 (2010).
[39] C. Moulsdale, A. Knothe, and V. Fal'ko, Phys. Rev. B **101**, 085118 (2020).
[40] C.-S. Park, Phys. Lett. A **382**, 121 (2018).
[41] J. N. Fuchs, F. Piéchon, M. O. Goerbig, and G. Montambaux, Eur. Phys. J. B **77**, 351 (2010).
[42] $|K^+\rangle$ is an ES of the QD at $\mathcal{N} = 1$ and finite $B_\perp$, which makes its occupations probability smaller than $|K^-\rangle$. Thus, most transitions originating from $|K^+\rangle$ are not clearly visible in the data, as their contribution to the transport current is much smaller.
[43] We cannot determine the sign of the coupling constants from comparison to the transport calculations. Changing the sign of $g_\perp, g_{z0}, g_{0z}$ reverses the order of states in the multiplets shown in Figs. 2(c),2(d) but leaves the pattern intact and hence leads to the same differential conductance maps as in Figs. 2(b).
[44] W. Albrecht, J. Moers, and B. Hermanns, J. Large-Scale Res. Facil. **3**, A112 (2017).